crystals

MDPI

Article

The Effect of Microstructural Evolution on the Brazeability of Two-Layer Al Sheets

Ting Yuan [1], Mingming Zuo [1], Zhipeng Yuan [2], Jingzhen Wang [3], Zili Liu [4], Quancheng Zhang [3,*] and Yiyou Tu [2,*]

[1] School of Materials Engineering, Changshu Institute of Technology, Changshu 215500, China
[2] School of Materials Science and Engineering, Southeast University, Nanjing 211100, China
[3] Jiangsu Alcha Aluminum Co., Ltd., Changshu 215500, China
[4] College of Materials Science and Technology, Nanjing University of Aeronautics and Astronautics, Nanjing 211100, China
* Correspondence: 201100009@cslg.edu.cn (Q.Z.); tuyiyou@seu.edu.cn (Y.T.)

Abstract: In this study, the microstructural evolution and the interaction between the clad and the core alloys that occurs during the brazing process of two-layer Al sheets with equiaxed grains were examined. The study was carried out using optical microscopy (OM), scanning electron microscopy (SEM), transmission electron microscopy (TEM), electron backscatter diffraction (EBSD) and glow discharge optical emission spectrometry (GDOES). The effects of microstructure on the brazing performances of two-layer sheets were clarified. Although the grains were fine and equiaxed before brazing, three typical microstructural evolutions happened during brazing, corresponding to three kinds of interactions between the clad and core alloys of the aluminum brazing sheets. In the alloys, which had either relatively uniform grain growth or no grain growth, the interaction between the clad alloy and the core alloy was weak; accordingly, they showed a smooth surface, an even microstructure, faint element mutual diffusion, and eventually good brazeability. Meanwhile, in the alloy with obvious abnormal grain growth (AGG), strain-induced liquid-film migration (SILFM) occurred when the energy was too low to cause strain-induced boundary migration (SIBM). This led to rough and uneven surface morphology, significant mutual diffusion, and surface segregation of elements; eventually, this produced the worst brazeability.

Keywords: microstructure; two-layer Al sheets; strain-induced boundary migration (SIBM); strain-induced liquid-film migration (SILFM); brazeability

Citation: Yuan, T.; Zuo, M.; Yuan, Z.; Wang, J.; Liu, Z.; Zhang, Q.; Tu, Y. The Effect of Microstructural Evolution on the Brazeability of Two-Layer Al Sheets. *Crystals* **2022**, *12*, 1387. https://doi.org/10.3390/cryst12101387

Academic Editor: Pavel Lukáč

Received: 13 September 2022
Accepted: 27 September 2022
Published: 29 September 2022

1. Introduction

Multilayer aluminum sheets are widely applied in the heat exchangers of air-conditioning systems due to their good formability, high thermal conductivity, and excellent corrosion resistance. In general, Al-Mn alloys are used to manufacture the core layer, and Al-Si alloys with low melting points are used as the clad layer. The properties of heat exchangers depend on the microstructural evolution of the chosen alloy during the brazing cycle, which enables fast and convenient brazing assembly of clad and core, forming a joint [1].

The temperature of the brazing process is generally controlled at about 600 °C under vacuum conditions; this is above the melting point for clad alloys and close to the melting point for core alloys. At such high temperatures, Al–Si clad alloys will completely melt and will flow above the core alloy due to the action of surface-tension forces. Although the core alloy remains solid, microstructural evolution inevitably occurs. The liquid films penetrate along the grain boundaries and precipitate to various depths into the core; this process is closely related to the amount of brazing and the formation of a successful joint [2].

The interaction between the clad and the core of multi-layered Al sheets has consistently attracted scientific interest. Yang [3] and Woods [3,4] first noted the phenomenon of

liquid-film migration (LFM) in strained Al brazing sheets and proposed three possible driving forces for LFM: (1) coherency strain energy; (2) reduction in particle matrix interfacial energy; and (3) reduction in energy in recovered dislocation structure or subgrain boundaries in the case of a slightly cold-worked brazing sheet. Wittebrood [5] recorded three kinds of interaction between the clad and the core of aluminum brazing sheets: no interaction, strain-induced boundary migration (SIBM) and strain-induced liquid-film migration (SILFM). The occurrence of SILFM indicates that the clad–core interaction is serious.

It has been shown that the clad-core interaction is strongly influenced by the microstructure of the core alloy. In general, an elongated, coarse, recrystallized structure being present before brazing reduces the number of grain boundaries, which is helpful for preventing the clad-core interaction. As a result, various approaches [6–8] have been studied to attain elongated, coarse, recrystallized grains. Kim et al. [9] investigated the effect of final rolling reduction on the grain-structure evolution of three-layered A4343(clad)/A3003(core)/A4343(clad) aluminum brazing sheets; they noticed that the core of the 44% cold-rolled sample was composed of coarse, elongated grains, which were free from any substructure. Yuan et al. [10] found that high-temperature (460 °C) final annealing significantly improved the brazing ability of 4343/3z23a/4343 multi-layered Al sheets and eliminated the erosion of the core layer during brazing.

However, large grain size is not beneficial for the mechanical properties or deep drawability of Al sheets. Studying the evolution of fine and equiaxed microstructures and their influence on the clad-core interaction during the brazing process remains an area of interest. In the present work, three types of two-layer sheets with equiaxed grains were studied; our aim was to investigate the relationships among the microstructural evolution, the interactions between the clad and the core, and the brazeability during the brazing process.

2. Materials and Methods

The experimental material was an AA4343/Mod3003 two-layer brazing sheet with a thickness of 1.35 mm. The core layer was a modified AA3003 aluminum alloy, and the clad layer, an AA4343 aluminum alloy, was present on one side of the sheet with a clad ratio of 5.8%.

The samples were obtained from Jiangsu Alcha Aluminum Co., Ltd. (Changshu, China) and were produced as follows: The core alloy and the clad alloy were each cast directly. After homogenization treatments, the core alloy was covered with the clad alloy and hot-rolled to a 7 mm thickness after a preheating treatment at 480 °C together. Then, the hot-rolled two-layer sheet was cold-rolled to the final thickness of 1.35 mm. The two-layer aluminum sheets were finally annealed at 360 °C for 15 h.

The homogenization treatment and the average chemical compositions of the experimental materials are listed in Tables 1 and 2, respectively. The core alloys, with different chemical compositions and different homogenization treatments are denoted as A, B, and C, respectively. As shown in Tables 1 and 2, samples A and sample C are processed by lower temperature homogenization treatment for their core alloys than that for sample B, and sheet C has much higher Fe and Si, but lower Mn than sheet A and B.

Table 1. Different homogenization annealing treatments of the experimental alloys.

Material	Processing	Homogenization Treatments
AA4343/Mod3003 two-layer brazing sheet	A	Annealed at 550 °C for 9 h
	B	Annealed at 590 °C for 9 h
	C	Annealed at 550 °C for 9 h

Table 2. Chemical composition (wt. %) of the experimental alloys.

Material	Fe	Si	Cu	Mn	Ti	Al
AA4343 (Clad)	0.176	7.76	0.220	0.022	0.017	Bal.
Mod3003 (Core) For sheet A and B	0.210	0.117	0.507	1.44	0.122	Bal.
Mod3003 (Core) Fore sheet C	0.441	0.719	0.592	1.23	0.142	Bal.

For simulating the brazing process, the samples were heated to 600 °C within 15 min and held for 5 min in the furnace under a vacuum condition of 10^{-3} Pa, then they were air-cooled to room temperature. The samples were placed vertically in the heating furnace to simulate the flow of a molten clad in the brazing process.

The surface morphologies of the sheets after brazing were observed with a three-dimensional digital microscope (VHX-5000, Keyence, Shanghai, China). The microstructures of the studied samples before and after brazing were examined by optical microscopy (OM, Olympus BX51), transmission electron microcopy (TEM, FEI Tecnai G2 T20, Hillsboro, OR, USA), and scanning electron microscopy (SEM, S3400N, Hitachi, Japan) with energy dispersive spectroscopy (EDS). The sheets for OM and SEM were wet-ground to 2000 grit, and polished and etched with a 0.5% hydrofluoric acid solution. Samples for TEM were prepared by mechanically polishing to ~60 μm; subsequently, an ion-thinning process was performed. Electron backscatter diffraction (EBSD) was also applied for a detailed characterization of the grain structures, and a map step size of 10 μm was used. The samples for the SEM, TEM, and EBSD observations were cut along the rolling direction, from the central region of the core alloy. Glow discharge optical emission spectrometry (GDOES, GDA 150 HR, Hof, Germany) was used to provide quantitative scans of the elements Si, Mn, Fe, and Cu with depth distributions. GDOES is a spectral-analysis technology based on the principle of inert gas discharge at low pressure. It is widely used in the characterization of the distribution of composition with depth in thin-film materials and functional multi-layer structures.

Electrical resistivity was measured to evaluate the variation in Mn in solid solutions during brazing, using a intelligent resistivity tester (TB300, Jinyang, Beijing, China) for the metal foil at room temperature.

In this paper, a method for testing the fluidity of the clad material by Jiangsu Alcha Aluminum Company Co., Ltd. was adopted [11]. The testing process for clad fluidity is shown in Table 3. The K value is used to characterize the fluidity of the brazing layer, and mainly depends on W_b, W_0 and Cl_r. It can be calculated as follows:

$$K = \frac{W_b - 0.25 \times W_0}{0.75 \times W_0 \times Cl_r} \quad (1)$$

where W_0 is the total weight of the sample after brazing, W_b is the weight of the bottom quarter of the sample after brazing, and Cl_r is a clad ratio of 5.8% in this paper. When $K \geq 0.2$, the fluidity of the brazing layer meets the requirements.

Table 3. The process of the fluidity test.

Stage	1	2	3	4
Temperature (°C)	RT-600	600	600–570	570-RT
Time (min)	17	10	Furnace cooling	Air cooling

3. Results

3.1. Primary Microstructures of Two-Layer Al Sheets before Brazing

3.1.1. Morphologies of Two-Layer Al Sheets before Brazing

Figure 1 shows the sectional morphologies of three two-layer Al sheets before brazing. As shown in Figure 1, a large number of Si particles were diffusely distributed in the clad layer prior to melting. The chemical concentration and the processing procedure for the clad material in the three two-layer Al sheets were the same. Consequently, there were nearly no differences in the volume fraction and distribution of the Si particles in the clad alloys of three sample sheets.

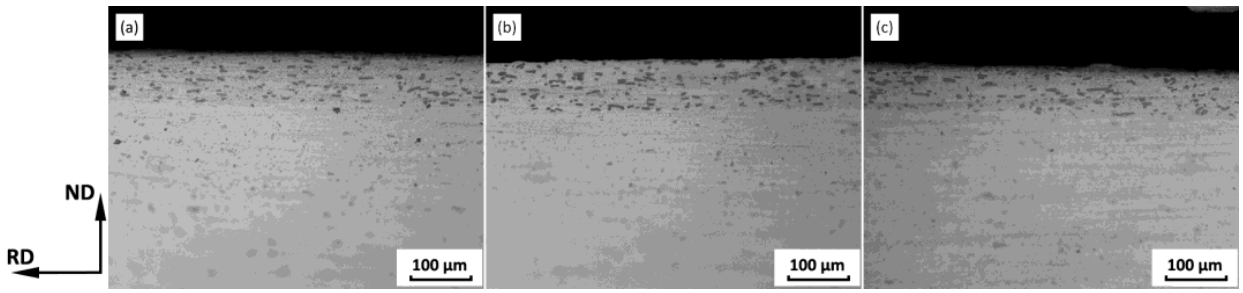

Figure 1. Optical microstructure of cross section of the brazing sheets before brazing, (**a**) Sample A, (**b**) Sample B, (**c**) Sample C.

3.1.2. Grain Structures of the Core Alloys before Brazing

The microstructure characteristics and grain-size distributions of the core alloys before brazing, as obtained by EBSD investigation, are shown in Figure 2. As shown in Figure 2, the microstructure was composed of equiaxed grains before brazing in the three different alloys. Sample A exhibited relatively coarse and unevenly distributed grains, as shown in Figure 2a. Compared with sample A, the grains in sample B and sample C were all fine grains with uniform distribution. As can be seen from Figure 2, before brazing, the grain sizes of the experimental sheet samples A, B, and C were determined to be 82 μm, 51 μm and 54 μm, respectively.

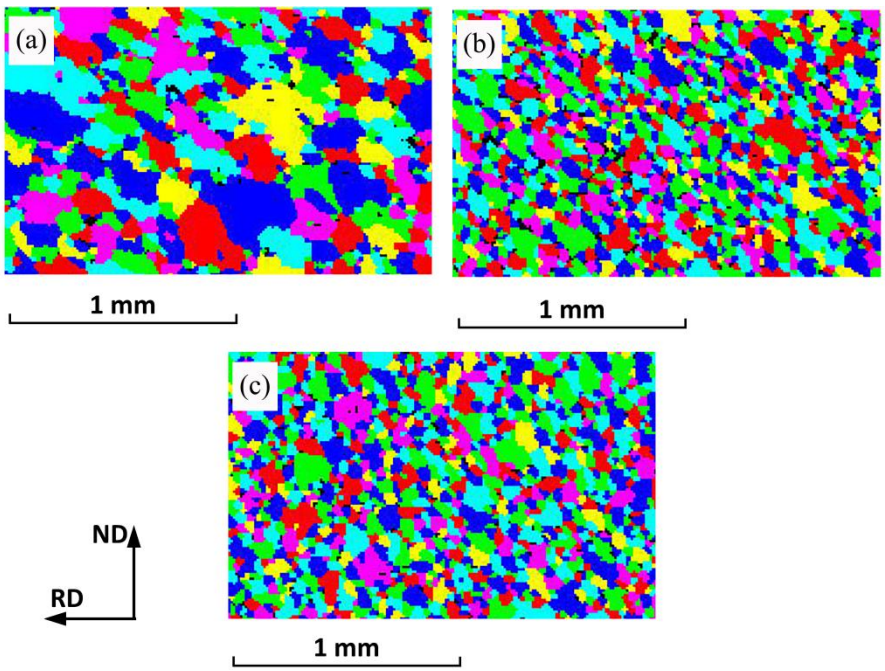

Figure 2. EBSD analysis of the three experimental alloys before brazing, (**a**) Sample A, (**b**) Sample B, (**c**) Sample C.

3.1.3. Primary Particles of the Core Alloys before Brazing

The precipitates in the core alloys before brazing are shown in Figure 3. A large quantity of fine, rod-like, and sphere-like dispersoids with an average particle size of 0.5 µm appeared in the matrix before brazing. Overall, the morphologies of the precipitates in the three alloys did not differ significantly. The dispersoids in alloy B were clearly fewer than those in alloys A and C, and their sizes were much larger, with occasional coarser ones with sizes above 1 µm. Figure 4 shows the SEM image and corresponding element distribution of the dispersoids in sample B. According to the EDS mapping, Mn and Fe elements were enriched in all dispersoids, and Si was distributed in some particles. As indicated, the particles were confirmed to be Al_6(Mn,Fe) together with α-Al(Mn,Fe)Si, which are both considered to be very important phases in 3xxx alloys [12]. A partly transformed "6-α" particle and clear duplex interfaces between different regions were also observed in the alloy. We note that some α-Al (Mn,Fe)Si particles nucleated at the interfaces of some primary Al_6(Mn,Fe) during homogenization [13].

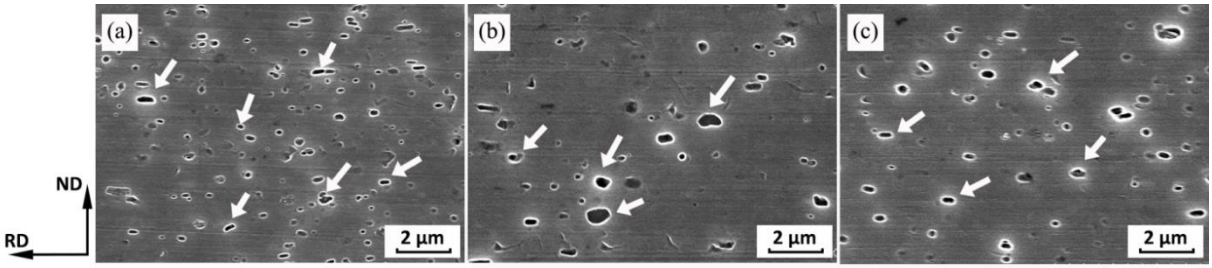

Figure 3. SEM microimages of the dispersoids in the core layer of three experimental alloys before brazing: (**a**) Sample A, (**b**) Sample B, (**c**) Sample C.

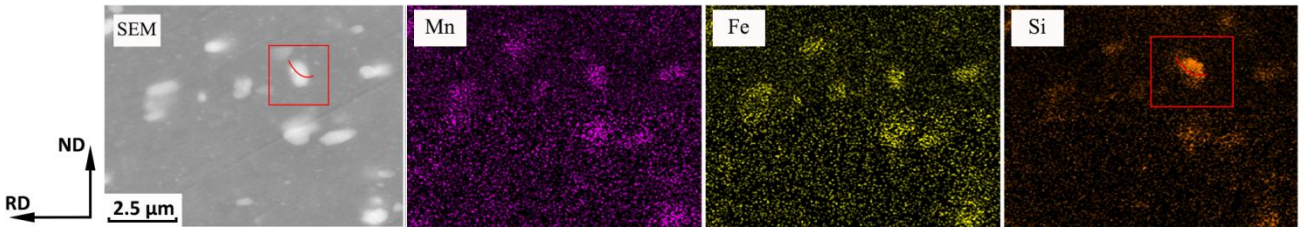

Figure 4. EDS mappings for the dispersoids in sample B.

3.2. Microstructure Evolutions of Two-Layer Al Sheets during Brazing

3.2.1. Morphologies of Two-Layer Al Sheets after Brazing

When the temperature was brought to 600 °C during the brazing process, the molten clad layer dissolved the core alloy. As a result, a re-solidified structure with large Al-Si grains, decorated by brick-like Si particles, was formed. The different morphologies of the three post-brazed specimens are shown in Figure 5. Among the three samples, the re-solidified clad of sample B held the highest amount of eutectic phase in, and the core material was attacked by the molten brazed clad alloy most remarkably in this sample. Furthermore, roughening of the surface was evident with some cavities in the clad alloy. This clearly shows the strong interaction between the molten clad alloy and the core alloy that occurred during brazing. In sample A, the eutectic structure largely remained near the sheet surface and appeared to be penetrating the core slightly. Meanwhile, in sample C, the Si particles appeared to be concentrated along the outermost surface of the clad layer; sample C had the lowest amount of Si particles. This reflects that the molten clad layer of sample C flowed away during the brazing process, resulting in a weak interaction with the core alloy [14].

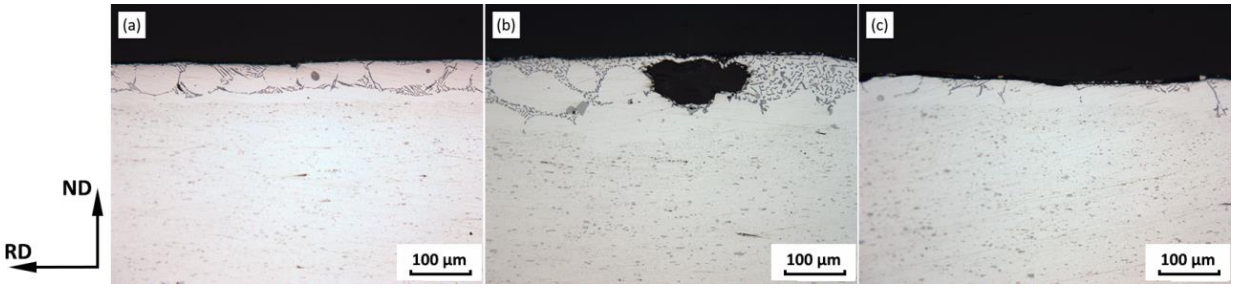

Figure 5. Optical microstructure of cross section of the brazing sheets after brazing, (**a**) Sample A, (**b**) Sample B, (**c**) Sample C.

Moreover, the re-solidified surface structures of the experimental sheets, along with the surface height, were examined by three-dimensional digital microscopy as shown in Figure 6. The left-hand figure for each sample shows the real morphology of the surface after brazing, while the right-hand figures show the heights of the surfaces which are marked by a blue line in the left-hand figures. As shown in the left-hand figures in Figure 6, the surface morphologies of samples A and C after brazing were relatively smooth, and their re-solidified structures were even across the whole surface. A minor height fluctuation can be observed in the right-hand figures of the two sheets. Compared with these two alloys, the surface morphology of sample B was much rougher, with many volcanic features unevenly distributed on the whole surface. The depth of the volcanic cavity was close to 80 microns. This agrees well with the roughness of the re-solidified sectional microstructure, as shown in Figure 5b, indicating a serious interaction between the clad and the core for sample B.

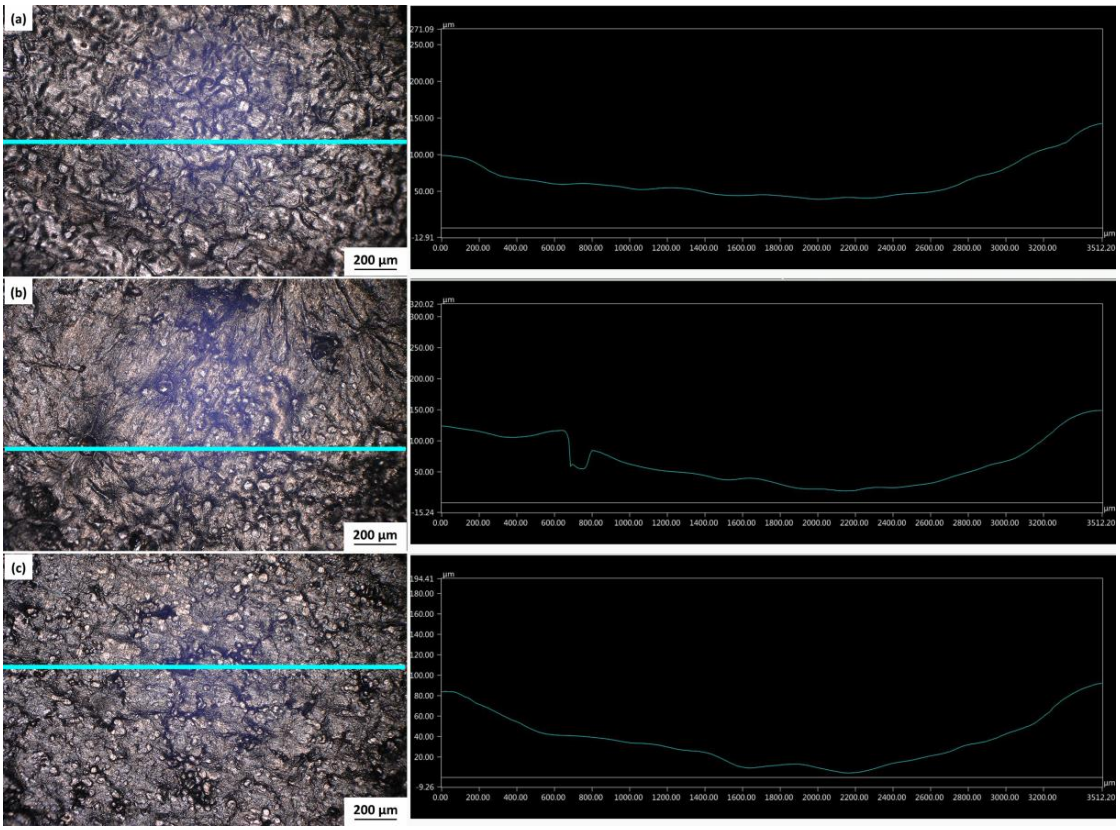

Figure 6. The re-solidified structure of the clad material after brazing, (**a**) Sample A, (**b**) Sample B, (**c**) Sample C.

3.2.2. Grain Structures of the Core Alloy after Brazing

The microstructure characteristics of the core alloys after brazing are shown in Figure 7. After brazing, the grain-structure evolution of the three experimental sheets was distinctly different. A coarser structure with sparse seldom local orientation spread was observed in sample A, suggesting that a relatively uniform coarsening took place. Although sample B showed a very small grain size before brazing, its growth rate was much faster than those of the other two samples. Figure 7b shows that a high density of remarkably elongated cell structures, with strong local orientation within grains, was observed in sample B. The original fine grain boundaries were penetrated by the abnormally coarse grains (as indicated by the arrows in Figure 7b). The distribution of grain size in sample B was quite heterogeneous after brazing, ranging from 40 to 800 μm in equivalent diameter. Considering the unique characteristics of the bimodal microstructure in sample B, we inferred that the grain growth was partially controlled by an abnormal mechanism [15]. Where the abnormal grain growth occurred, the grain size reached up to several hundred micrometers and a few millimeters. For sample A, grains with sizes above 200 μm dominated the microstructure, while grains in the range of 20–200 μm primarily existed in the form of island grains, or sandwiched between large grains (as indicated by the arrows in Figure 7a). In sample B, grains larger than 400 μm were infrequent, comprising half the area, while grains smaller than 200 μm were more frequent, comprising the other half of the area. Compared with samples A and sample B, sample C showed remaining fine and quasi-equiaxed grains. Figure 7c indicates that there was little grain growth, with the average grain size increasing from 54 to 68 μm.

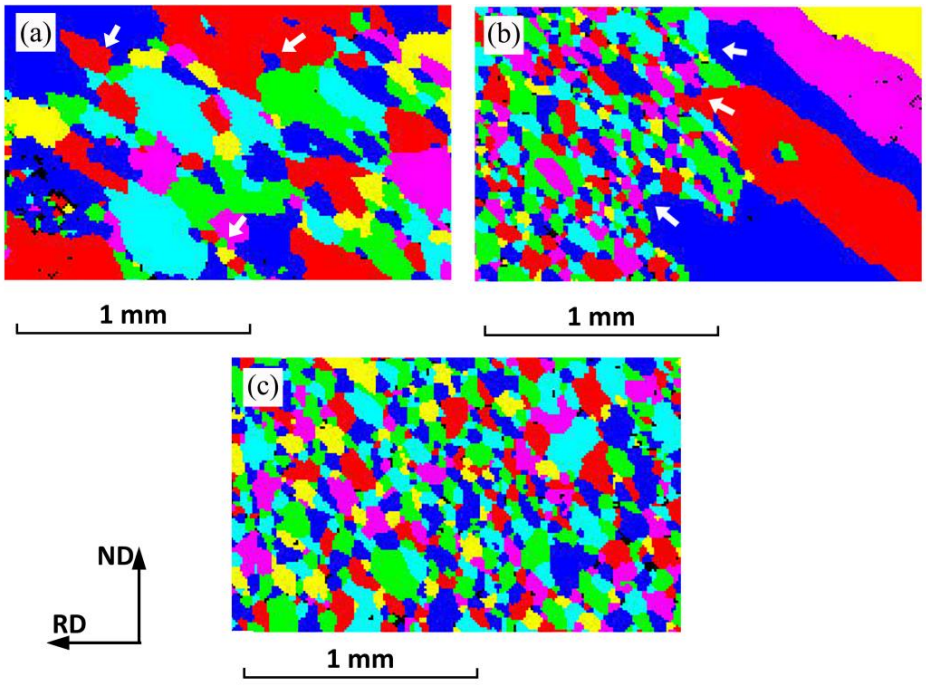

Figure 7. EBSD analysis of the three experimental alloys after brazing, (**a**) Sample A, (**b**) Sample B, (**c**) Sample C.

In summary, during the high-temperature brazing, a relatively uniform grain growth phenomenon was observed in sample A, a significant abnormal grain growth (AGG) phenomenon occurred in sample B, and the microstructure of sample C remained fine and uniform.

3.2.3. Precipitates of the Core Alloys after Brazing

The morphologies of the precipitates in the core alloys after brazing are shown in Figure 8. After brazing, a slight coarsening but remarkable dissolution of the precipitates

took place, as implied by the smaller population but larger size of the precipitates after brazing compared with those before brazing. The decline in the number density and the increase in the size of these precipitates were most significant in samples A and B, but less distinct in sample C.

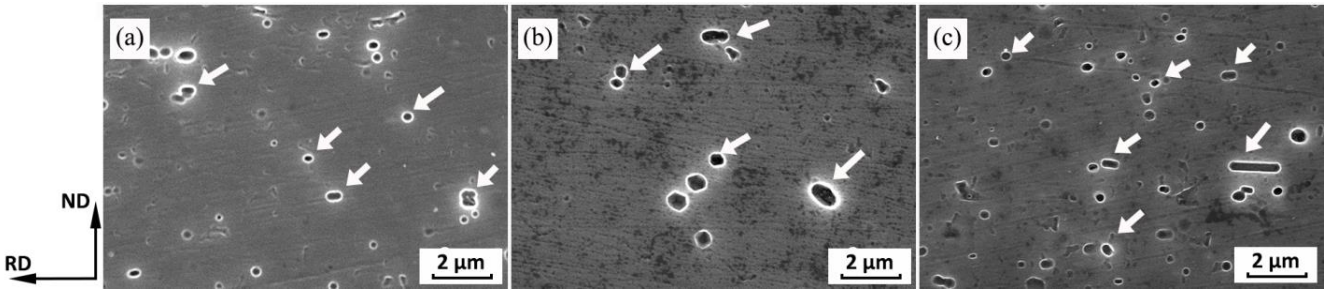

Figure 8. SEM microimages of the precipitate evolution in the core layer of three experimental alloys after brazing: (**a**) Sample A, (**b**) Sample B, (**c**) Sample C.

Figure 9 shows TEM images of the precipitates after brazing at 600 °C. Many fine rod-like and spherical-like precipitates were visible in the matrix. Since the applied HF etching leads to an apparent enlargement of the etched particles, the TEM micrographs reveal smaller, more realistic, particle sizes of the precipitates than the SEM micrographs. The morphology of the precipitates in the three samples did not differ significantly. However, the number of fine precipitates in sample C was clearly greater than that in the other two alloys. Additionally, the precipitates in sample B were large in size. This observation is generally associated with higher Fe and Si contents, as seen in sample C. It is well known that higher Si and Fe concentrations results in lower Mn concentrations in solid solutions, and these promote the precipitation of Mn from the matrix during high-temperature treatments [16]. As a result, the microstructure of sample C after brazing was characterized by the highest number of dispersoids, which were the finest in size, compared with the other two experimental sheets.

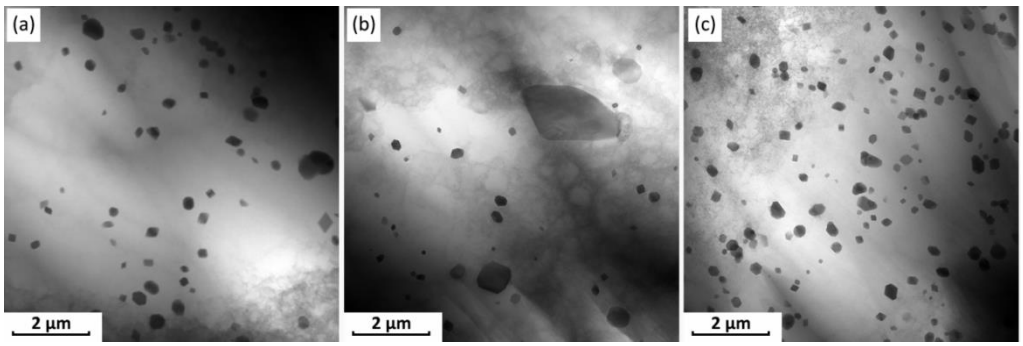

Figure 9. TEM images of the precipitates after brazing at 600 °C in (**a**) sample A, (**b**) sample B, and (**c**) sample C.

The STEM-EDX mapping results presented in Figure 10a revealed these small precipitates to be α-Al(Mn,Fe)Si. Figure 10b shows a high resolution (HR)TEM image of the precipitates and Figure 10c exhibits an enlarged HRTEM image in the frame inserted in b. The interface between the precipitates and the Al phase can be identified by the HRTEM and corresponding IFFT images in Figure 10c,d. From Figure 10c, we can see that the interlayer spacing of the matrix was 0.2009 nm, which corresponded to the (200) lattice plane spacing for the Al phase; meanwhile, the interlayer spacing of the precipitates was 0.3747 nm, which corresponded to the (110) lattice plane spacing for the α-Al(Mn,Fe)Si phase. It should be noted that, interestingly, the misfit dislocations accumulated mostly

between the precipitates and the Al matrix; this could be very effective in impeding the movement of dislocations and grain boundaries to different extents [17].

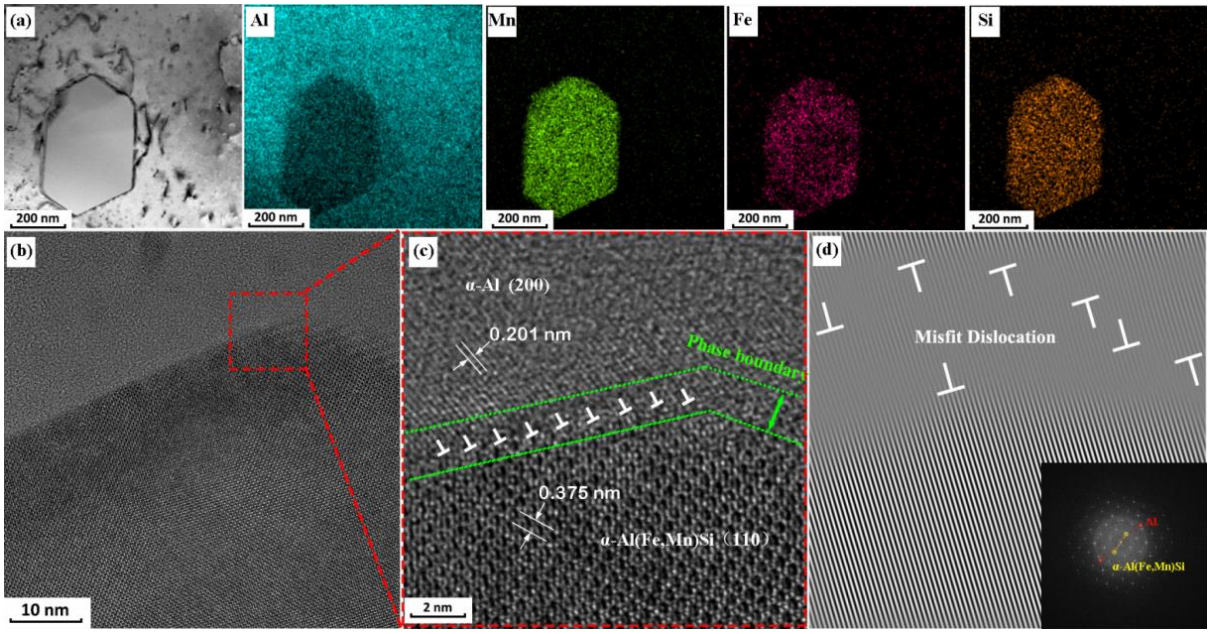

Figure 10. HRTEM and associated IFFT images of α-Al(Mn,Fe)Si precipitate in sample C: (**a**) HAADF-STEM image of α-Al(Mn,Fe)Si precipitate with corresponding STEM-EDX elemental mapping; (**b**) HRTEM image shows the interface between the precipitate and the Al matrix; (**c**) enlarged HRTEM image in the frame inserted in (**b**) showing the interface between Al and α-Al(Mn,Fe)Si precipitate with periodically spaced misfit dislocations; (**d**) was obtained after Fast Fourier Transformation (FFT) and inverse FFT in order to show misfit dislocations, the corresponding FFT of Al and α-Al(Mn,Fe)Si phase as inset.

3.3. Electrical Resistivity Evolution during Brazing

The relationship between electrical resistivity, ρ, of the alloy and the alloying elements content in the solid solution can be expressed as [12,17]:

$$\rho = 0.0267 + 0.033\ w(\mathrm{Mn}) + 0.032\ w(\mathrm{Fe}) + 0.0068\ w(\mathrm{Si}) + 0.0032\ w(\mathrm{Cu}) \quad (2)$$

where w(Mn), w(Fe), w(Si) and w(Cu) are the weight percentages of Mn, Fe, Si, and Cu in the solid solution, respectively. As can be seen from Equation (2), w(Fe), w(Si), and w(Cu) have much less influence on electrical resistivity compared with w(Mn). In addition, the present alloy contains low concentrations of Fe, Si, and Cu. In the 3xxx alloy, we observed that nearly all the Fe content formed intermetallic particles during solidification, and their concentrations in solid solutions varied little during heat treatment. Thus, the electrical resistivity of the experimental alloy was dominantly controlled by the level of Mn in the solid solution. The evolution of ρ can be used to obtain a detailed indication of the dissolution of Mn from the supersaturated solid solution during brazing. Figure 11 shows the electrical resistivity evolution of the experimental alloys during the brazing treatment. After the alloy was brazed at 600 °C, there was a remarkable increase in electrical resistivity. This resulted from the increase in the solute concentration of Mn due to the dissolution of dispersoids into the matrix. As clearly demonstrated in Figure 11, the electrical resistivity of alloy B was the highest, since it contains a high Mn content but the fewest Mn-containing particles both before and after brazing. Sample C showed the lowest electrical resistivity compared with the other two alloys based on Equation (2), owing to its lower concentration of Mn and much higher weight percentage comprised of Fe and Si. This agreed well with the SEM observation of the dispersoid evolution, as shown in Figure 8.

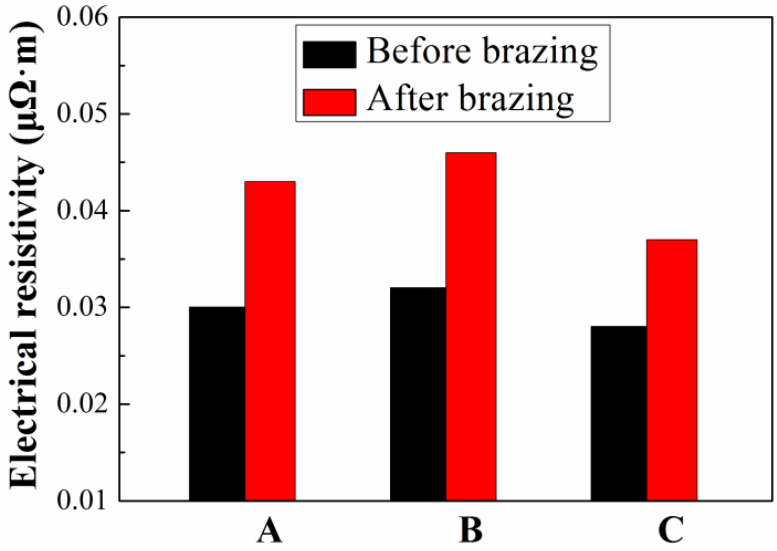

Figure 11. Electrical resistivity evolution of experimental alloys during brazing. A, B, C in the figure represent sample A, sample B and sample C.

3.4. Element Diffusion between the Core and the Clad during Brazing

Element diffusions near the interface between the core and the clad during high-temperature brazing were studied by quantitative GDOES analysis, as shown in Figure 12. The distributions of the elements before brazing in the three samples were the same. As can be seen from Figure 12, before brazing, there was a clear interface between the clad material and the core material at the depth of about 60 μm. The content of Mn in the core layer of sheet C was lower than that of sheets A and B, and the contents of Si and Fe were higher; this was in good agreement with the chemical compositions of the alloys. During high-temperature brazing, the elements in the clad and the core diffused into each other, driven by the concentration gradient [18]. The interface between the clad and the core became unclear after brazing, as displayed in Figure 12. The Si concentration was reduced in the re-solidified clad material, but the mass fraction of Si along the outmost surface increased significantly to above 10 wt.%. After brazing, the Cu diffused from the core alloy into the clad alloy, and element enrichment was observed in the re-solidified clad material. Fe, Mn, and Cu in sample B were all highly enriched near the surface, especially the mass fraction of Cu, which increased to about 1.0 wt.%. Comparing the three experimental samples, the mutual diffusion and surface segregation of the elements in sheet B were the most significant, indicating the presence of the strongest interaction between the core and the clad in sample B; this result was in full accordance with the initial observations of this study.

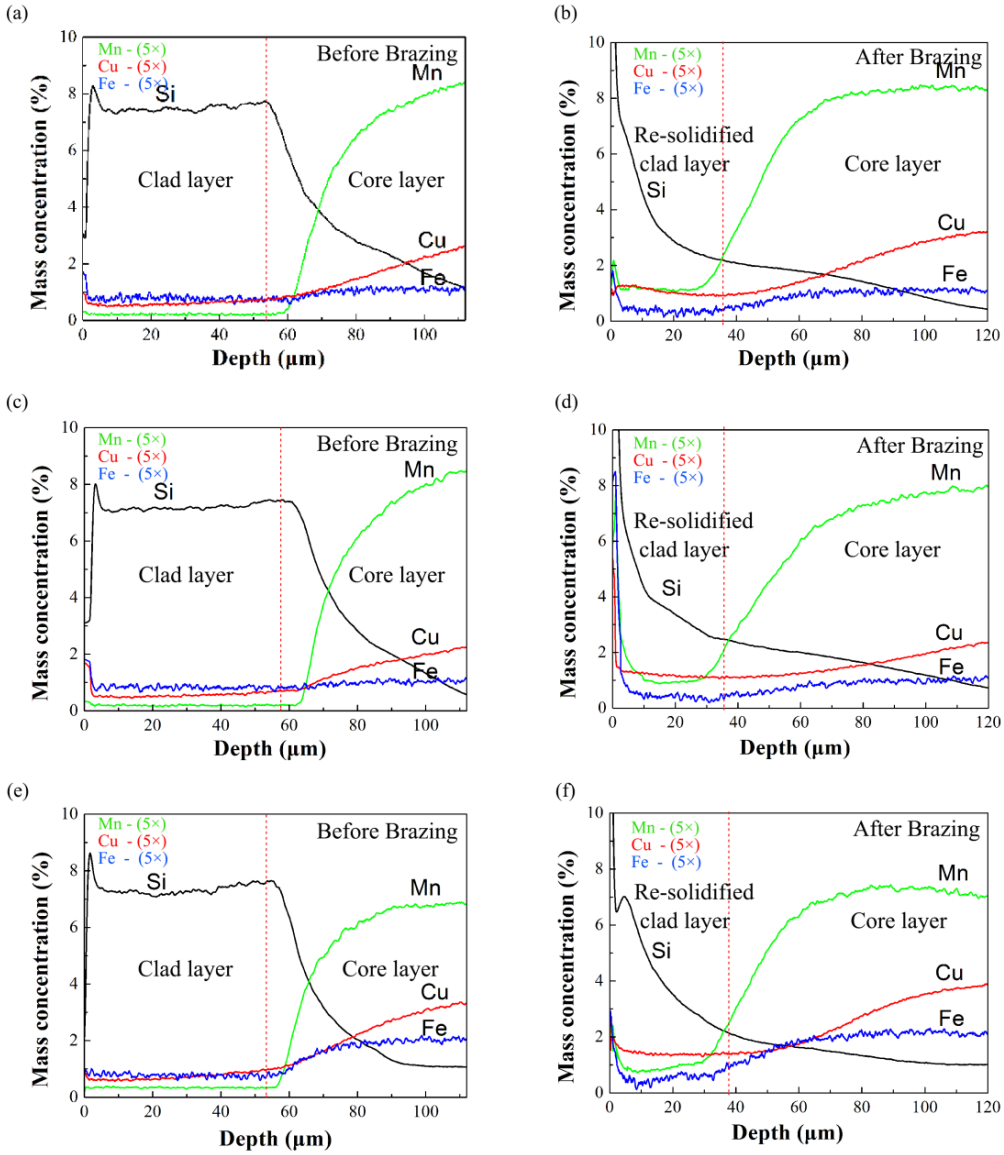

Figure 12. GDOES profiles of the three experimental alloys (**a**,**c**,**e**) before and (**b**,**d**,**f**) after brazing, (**a**,**b**) Sample A, (**c**,**d**) Sample B, (**e**,**f**) Sample C. The red-dotted line in the figures represents the interface between the clad material and the core material. (Due to the huge difference between the contents of different elements, the mass concentrations of Mn, Fe and Cu in the figures are magnified by 5 times).

4. Discussion

4.1. The Microstructural Evolution during Brazing for the Two-Layer Sheets

Here, we provide a brief discussion of the mechanisms of the microstructural evolution which occurred in the three samples during the brazing process. Before brazing, the density and size of the particles in the samples mainly depended on the processing parameters, such as the homogenization temperature and the chemical compositions. It is well known that coarsening and dissolution are the two most prominent processes which occur during high-temperature treatments, because the high diffusion rate which increasing temperature induced in elements makes long distance diffusion possible. According to Li et al. [12], the electrical resistivity achieves a minimum at about 530 °C and then increases with temperature, due to the dissolution of Mn-containing dispersoids into the matrix, which makes the solute concentration of Mn increase. Since the temperature of the homogenization treatment used for sample B was 590 °C, much higher than that used for samples A and

C, the Mn-containing particles for sample B were much fewer in number as indicated in Figure 3b, indicating that sample B possessed the highest electrical resistivity.

Due to the high temperature but short duration of brazing process, long distance diffusion of Mn is difficult during brazing. Thus, dissolution becomes the dominant mechanism during brazing. As indicated in Figure 8, during brazing, a remarkable decrease but slight coarsening in precipitation took place in samples A and B. The remarkably reduction in number density of the Mn-containing particles greatly increased the solute concentration of Mn in the solid solution. Although the size of some Mn-containing particles slightly increased, only a small amount of Mn was consumed because the duration of the brazing process was too short to allow a large amount of Mn to diffuse. Therefore, the electrical resistivity increases after brazing. However, it is worth noting that little change in precipitations occurred in sample C; this finding is mainly associated with the much higher content of Fe and Si in sample C than in the other two samples. The different levels of added alloying elements in the core alloy has a strong influence on the precipitation behavior of that alloy. Fe and Si greatly decreased the solute concentration of Mn in the solid solution and accelerated the precipitation rate; the resultant effects of this may lead to the most— but slightly coarsened— precipitations in sample C after brazing.

It is well known that precipitation has a large influence on the recrystallization and the final microstructure of alloys [19,20]. Smaller particles of sizes <1 μm may contribute to the pinning effect (Zener pinning) on grain boundaries, while larger particles of sizes >1 μm may act as active sites for the nucleation of recrystallization. Differences in the extent of precipitation in the three experimental two-layer sheets played an important role in the microstructural evolution that occurred during the brazing process, and had a close association with secondary recrystallization and abnormal grain growth (AGG) in this study [21].

In sample A, a clear decrease in the precipitates occurred during brazing, reducing the pinning of the low-angle and high-angle boundaries. It can be seen from Figure 13a that the boundary of recrystallized grain A was bowed out toward the region with higher dislocation density, and bulged inward toward the pre-existing grain boundary, leaving a dislocation-free region behind the migrating boundary. This was supposed to be an example of strain-induced boundary migration (SIBM). It can be seen from Figure 13b that the angle of the triple junction was about 120°, indicating that a fully recrystallized microstructure was obtained, which transitioned the grain boundaries into an equilibrium state.

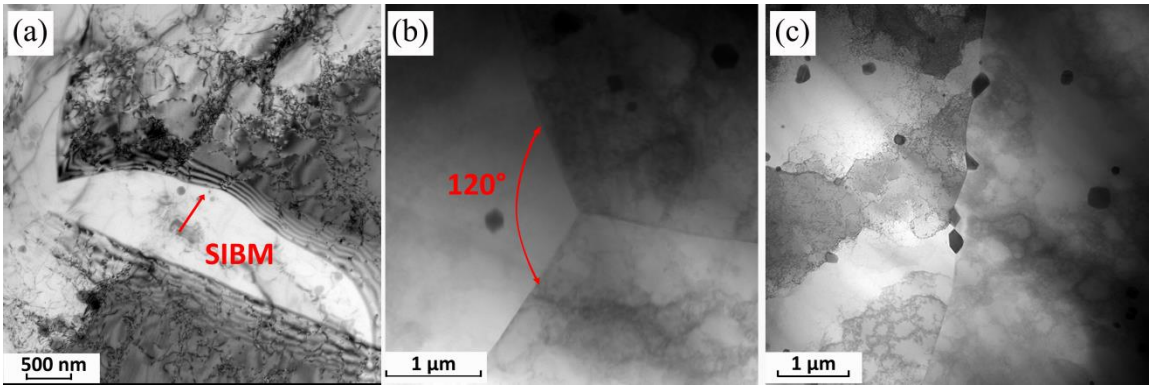

Figure 13. TEM observations of (**a**,**b**) SIBM and triple grain boundary in sample A; (**c**) Bright field images showing precipitates in aluminum grains and in the grain boundary of sample C.

In sample B, although the microstructure was fine and uniform before brazing—a result of large particles (>1 μm) acting as active sites for the nucleation of recrystallization—AGG occurred during high-temperature brazing, as shown in Figure 7b. Both the dissolution of the large precipitates and the lack of fine dispersoids reduced the barrier to the migrated grain boundary, which seemed to be involved in triggering AGG [22]. Many grain-boundary particles dissolved with the increase in temperature, and the dislocations that occurred in the grain boundaries were

released and consumed. Vollmer et al. [23] found that the dissolution of particles is related to the misorientation gradient of some grains, which can also promote the AGG process. Generally, two possible mechanisms can be attributed to AGG: (1) nucleation-limited recrystallization and (2) the heterogeneity of the distribution of stored energy [24]. Since there are few small particles of sizes <1 μm which contributed to the pinning effect (Zener pinning) of grain boundaries, the main mechanism for AGG in this study was a heterogeneous distribution of stored energy. Some grains might contain more stored energy than their neighboring grains; these can be absorbed by those lower-stored-energy neighboring grains, which then grow abnormal-growth grains. When AGG starts, the migration and annihilation of dislocations repeated inside equiaxed grains, resulting in the coalescence of subgrains and the progression of AGG. Therefore, with the dislocations gliding through the entire grain and annihilating again and again, most subgrain structures are swept out by the migration of dislocations, and the low-angle grain boundaries (LAGBs) decrease gradually during this process. The fine subgrains merge into coarse grains, making most of the grain boundaries disappear. Then, the growth of abnormal grains grants them a size advantage over their neighboring grains, which, in turn, acquire more driving force to grow themselves [25].

Meanwhile, in sample C, many small dispersoids remained in the matrix after brazing. As shown in Figure 13c, the grain boundaries were pinned by those dispersoids. Blocked bowing dislocations were observed, and they accumulated around the particles, which were confirmed to be α-Al(Mn,Fe)Si by the STEM-EDX mapping results. Sample C had the highest volume fractions of precipitates after brazing; thus, the α-Al(Mn,Fe)Si precipitates should have provided the strongest recrystallization resistance, which suppressed severe grain growth and resulted in fine, equiaxed grains in sample C. The high density of precipitates in the alloy after brazing can be attributed to the high Si content in the core of sample C.

4.2. The Effect of Microstructure on the Brazeability of the Two-Layer Sheet

The entirely different microstructural evolutions had a significant impact on the interaction between the clad alloys and the core alloys, and then affected the brazing performances of the two-layer Al sheets. The fluidity of the clad material was tested to evaluate the brazeability of the two-layer sheets, which is presented in Table 4. The macrophotographs of the samples after the fluidity test are exhibited in Figure 14. The calculated K values of samples A, B, and C are 0.20, 0.05, and 0.25, respectively. Thus, the fluidity of brazing sheet sample C was the best among the three samples, followed by sample A; the fluidity of brazing sheet sample B was evidently the worst. This indicates that the molten clad of sample B didn't flow away and remained along the surface during the brazing process. As a result, the core alloy was seriously corroded by the molten clad. These results were in full accordance with the previous observations of this study. Since there was a strong interaction between the molten clad alloy and the core alloy in sample B during brazing, the surface was terribly rough after brazing, as shown in Figure 14. The amount of brazing may have reduced, and led to a less successful joining. On the other hand, the clad alloys of samples A and C had good fluidity, so that the interaction with the core alloy was the smallest. Thus, there was a substantial amount of re-solidified clad material at the bottom of samples A and C after brazing, as displayed in the rectangle in Figure 14. Samples with sufficient liquid formation formed a complete bond, presenting a good brazing performance.

Table 4. The calculated fluidity coefficient K of the clad material of the experimental sheets.

Materials	Cl_r	W_o	W_b	K
A	0.058	25.32	6.55	0.20
B	0.058	25.29	6.39	0.06
C	0.058	25.19	6.57	0.25

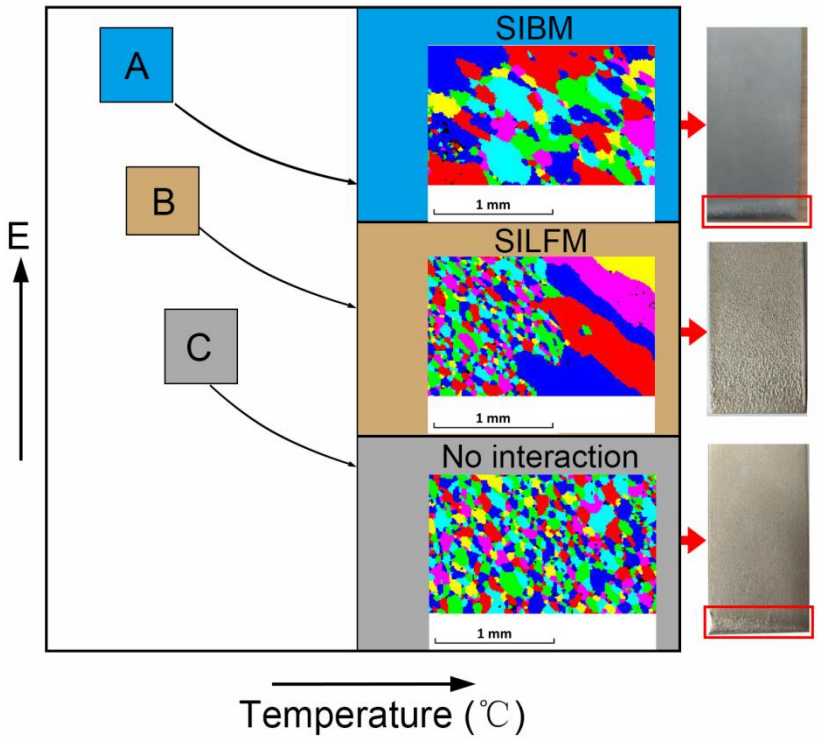

Figure 14. The microstructural evolution and the brazing performance of the two-layer Al sheets after fluidity test. A, B, C in the figure represent sample A, sample B and sample C.

The relationship between the microstructural evolution and the brazing performance of the two-layer Al sheets can be explained by the interaction mechanism of the clad and the core alloys, as shown in Figure 14. The "E" on the y-axis represents the residual energy in the core alloy in the Al sheets before brazing. As stated by Wittebrood [5], there are three kinds of interaction between the clad and core: no interaction, SIBM and SILFM. During brazing process, SIBM and SILFM are in competition with each other because they use the same source of energy. The core of sample A shows obvious signs of recrystallization by SIBM. This takes away the energy which might otherwise be available to cause SILFM during brazing. Meanwhile, the core of sample C showed little change in microstructure, indicating that there was not enough energy to induce SIBM or SILFM. Under these two conditions, there was no obvious interaction between the molten clad and the solid core material except solid element diffusion. As a result, samples A and C showed good brazeability, presenting the best fluidity of the clad material as indicated in Table 4. As shown in Figure 14, the brazed surfaces of samples A and C are both smooth, with a sufficient brazed joint at the bottom of the sheets.

However, AGG occurred in sample B. The driving force of this kind of AGG is the stored energy difference across the grain boundary [26]. Therefore, the stored energy distribution is thought to have been heterogeneous in sample B, which could have had a great impact on the SIBM and SILFM processes. When stored energy is high, SIBM occurs, leading to extremely coarse grains. When stored energy is too low to cause SIBM, SILFM occurs. As a result, SILFM happened with AGG in sample B. When SILFM occurs, the liquid molten clad layer significantly dissolves the core layer, resulting in an uneven, rough surface morphology and a reduced amount of braze after solidification. As indicated in Figure 14, very little re-solidified clad material formed at the bottom of the sheet. This was in good agreement with the increased volume of the dendritic structure, the significant inter-diffusion, and the surface segregation which were observed in sample B. Consequently, sample B had the worst fluidity among the clad materials, leading to poor brazeability.

5. Conclusions

In this study, the microstructures and the mutual interactions between the clad and the core of different two-layer Al sheets were clarified by SEM, TEM, EBSD, and GDOES. Additionally, the effects of microstructures on the brazing performances of two-layer sheets were investigated. The following conclusions were drawn from the findings of this study:

(1) During brazing process, the molten cladding layer of the two-layer Al sheet dissolved the core alloy and showed an interaction with the latter. Sample B had the most significant eutectic phase in the re-solidified clad alloy, the worst fluidity of the molten clad alloy, and the most rough and uneven surface morphology after brazing; these findings indicated that sample B showed the strongest interaction between the core and the clad alloys. Significant mutual diffusion and surface segregation of the elements in sheet B were observed.

(2) Although the microstructures in the three different two-layer sheets were all fine and uniform before brazing, different phenomena occurred during the brazing processes of each: relatively uniform grain growth, significant AGG, and no grain growth. The AGG phenomenon was related to the heterogeneous distribution of stored energy and the dissolution of the precipitates in the core alloy.

(3) Three kinds of microstructural evolution corresponded to three kinds of interaction between the clad and core alloys of the aluminum brazing sheets. SIBM took place in the alloy with relatively uniform grain growth. The alloy with no grain growth did not have enough energy to induce SIBM or SILFM. In the alloy with AGG, SILFM occurred when the energy was too low to cause SIBM, leading to this alloy having the worst brazeability.

Author Contributions: The work presented here was carried out in collaboration between all authors. Q.Z. and Z.L. defined the research theme; T.Y. and J.W. performed the main experiments; T.Y. and Z.Y. analyzed the data and wrote the main draft of the paper; M.Z. and Y.T. co-designed experiments, discussed the analysis, and revised the manuscript. All authors have read and agreed to the published version of the manuscript.

Funding: This research was funded by the Science & Technology Plan Project of Jiangsu Province of China (Grant No. SBA2020030289).

Institutional Review Board Statement: Not applicable.

Informed Consent Statement: Not applicable.

Data Availability Statement: The data presented in this study are available upon request from the corresponding author.

Conflicts of Interest: The authors declare no conflict of interest.

References

1. Ryu, J.-S.; Kim, M.-S.; Jung, D. Brazeability of cold rolled three layer Al–7.5Si/Al–1.2Mn–2Zn–(0.04–1.0)Si/Al–7.5Si (wt.%) clad sheets. *J. Mater. Process. Technol.* **2002**, *130–131*, 240–244. [CrossRef]
2. Qin, J.; Kang, S.-B.; Cho, J.-H. Sagging mechanisms in the brazing of aluminum heat exchangers. *Scr. Mater.* **2013**, *68*, 941–944. [CrossRef]
3. Yang, H.S.; Woods, R.A. *Mechanisms of Liquid Film Migration (LFM) in Aluminum Brazing Sheet*; SAE International: Warrendale, PA, USA, 1997.
4. Woods, R.A. *Liquid Film Migration During Aluminum Brazing*; SAE International: Warrendale, PA, USA, 1997.
5. Wittebrood, A.J. Microstructural Changes in Brazing Sheet due to Solid-Liquid Interaction. Doctoral Thesis, Technische Universiteit, Delft, The Netherlands, 2009.
6. Tang, D.; Fan, X.; Fang, W.; Li, D.; Peng, Y.; Wang, H. Microstructure and mechanical properties development of micro channel tubes in extrusion, rolling and brazing. *Mater. Charact.* **2018**, *142*, 449–457. [CrossRef]
7. Benoit, M.J.; Whitney, M.A.; Wells, M.A.; Jin, H.; Winkler, S. Liquid Film Migration in Warm Formed Aluminum Brazing Sheet. *Metall. Mater. Trans. A* **2017**, *48*, 4645–4654. [CrossRef]
8. Tu, Y.Y.; Liu, X.L.; Zhang, M.D.; Zhang, J.J. Improving Brazeability of AA3003+Zn Brazing Aluminum Sheets by Final Annealing. *Adv. Mater. Res.* **2011**, *197–198*, 1555–1560. [CrossRef]

9. Kim, S.-H.; Kang, J.-H.; Euh, K.; Kim, H.-W. Grain-structure evolution of brazing-treated A4343/A3003/A4343 aluminum brazing sheets rolled with different reductions. *Met. Mater. Int.* **2015**, *21*, 276–285. [CrossRef]
10. Yuan, Z.; Tu, Y.; He, H.; Yuan, T.; Zhang, Q.; Peng, X. Influence of final annealing temperature on the microstructural evolution and corrosion resistance of a Sandwich multi-layered aluminum sheet. *Mater. Res. Express* **2018**, *6*, 026536. [CrossRef]
11. Yuan, Z.; Tao, F.; Wen, J.; Tu, Y. The Dependence of Microstructural Evolution and Corrosion Resistance of a Sandwich Multi-Layers Brazing Sheets on the Homogenization Annealing. *IEEE Access* **2019**, *7*, 121388–121394. [CrossRef]
12. Li, Y.J.; Arnberg, L. Quantitative study on the precipitation behavior of dispersoids in DC-cast AA3003 alloy during heating and homogenization. *Acta Mater.* **2003**, *51*, 3415–3428. [CrossRef]
13. Alexander, D.T.L.; Greer, A.L. Solid-state intermetallic phase tranformations in 3XXX aluminum alloys. *Acta Mater.* **2002**, *50*, 2571–2583. [CrossRef]
14. Benoit, M.J.; Whitney, M.A.; Wells, M.A.; Winkler, S. Effect of Temperature and Sheet Temper on Isothermal Solidification Kinetics in Clad Aluminum Brazing Sheet. *Metall. Mater. Trans. A* **2016**, *47*, 4425–4436. [CrossRef]
15. Na, T.-W.; Park, H.-K.; Park, C.-S.; Park, J.-T.; Hwang, N.-M. Misorientation angle analysis near the growth front of abnormally growing grains in 5052 aluminum alloy. *Acta Mater.* **2016**, *115*, 224–229. [CrossRef]
16. Yuan, Z.; Tu, Y.; Yuan, T.; Huang, Y.; Zhang, Y. Effect of the interaction between Fe and Si on the precipitation behavior of dispersoids in Al–Mn alloys during homogenization. *Vacuum* **2021**, *184*, 109915. [CrossRef]
17. Long, L.; Pan, Q.; Li, M.; Ye, J.; Sun, Y.; Wang, W.; Luo, Y.; Li, X.; Peng, Z.; Liu, S. Study on microstructure and mechanical properties of 3003 alloys with scandium and copper addition. *Vacuum* **2020**, *173*, 109112. [CrossRef]
18. Yuan, T.; Zhang, M.-D.; Ni, J.-H.; Chen, Y.-X.; Geng, F. The brazing effect on the corrosion mechanism of a multilayer material with Cu. *Anti-Corros. Methods Mater.* **2017**, *64*, 664–671. [CrossRef]
19. Bennett, T.A.; Petrov, R.H.; Kestens, L.A.I.; Zhuang, L.Z.; de Smet, P. The effect of particle-stimulated nucleation on texture banding in an aluminum alloy. *Scr. Mater.* **2010**, *63*, 461–464. [CrossRef]
20. Tu, Y.; Qian, H.; Zhou, X.; Jiang, J. Effect of Scandium on the Interaction of Concurrent Precipitation and Recrystallization in Commercial AA3003 Aluminum Alloy. *Metall. Mater. Trans. A* **2013**, *45*, 1883–1891. [CrossRef]
21. Yang, C.; Baker, I. Effect of soluble particles on microstructural evolution during directional recrystallization. *Acta Mater.* **2020**, *188*, 288–301. [CrossRef]
22. Xu, X.; Ma, X.; Zhao, G.; Chen, X.; Wang, Y. Abnormal grain growth of 2196 Al-Cu-Li alloy weld seams during extrusion and heat treatment. *J. Alloys Compd.* **2021**, *867*, 159043. [CrossRef]
23. Vollmer, M.; Arold, T.; Kriegel, M.J.; Klemm, V.; Degener, S.; Freudenberger, J.; Niendorf, T. Promoting abnormal grain growth in Fe-based shape memory alloys through compositional adjustments. *Nat. Commun.* **2019**, *10*, 2337. [CrossRef]
24. Wang, X.; Huang, Z.; Cai, B.; Zhou, N.; Magdysyuk, O.; Gao, Y.; Srivatsa, S.; Tan, L.; Jiang, L. Formation mechanism of abnormally large grains in a polycrystalline nickel-based superalloy during heat treatment processing. *Acta Mater.* **2019**, *168*, 287–298. [CrossRef]
25. Rios, P.R.; Gottstein, G. Texture evolution during normal and abnormal grain growth in an Al–1 wt% Mn alloy. *Acta Mater.* **2001**, *49*, 2511–2518. [CrossRef]
26. Agnoli, A.; Bernacki, M.; Logé, R.; Franchet, J.-M.; Laigo, J.; Bozzolo, N. Selective Growth of Low Stored Energy Grains During δ Sub-solvus Annealing in the Inconel 718 Nickel-Based Superalloy. *Metall. Mater. Trans. A* **2015**, *46*, 4405–4421. [CrossRef]